This document is the accepted manuscript version of the following article:
Mishra, S., Beyer, D., Eimre, K., Kezilebieke, S., Berger, R., Gröning, O., … Fasel, R. (2019). Topological frustration induces unconventional magnetism in a nanographene. Nature Nanotechnology. https://doi.org/10.1038/s41565-019-0577-9

Topological frustration induces unconventional magnetism in a nanographene

Shantanu Mishra[1]†, Doreen Beyer[2]†, Kristjan Eimre[1], Shawulienu Kezilebieke[3], Reinhard Berger[2], Oliver Gröning[1], Carlo A. Pignedoli[1], Klaus Müllen[4], Peter Liljeroth[3], Pascal Ruffieux[1], Xinliang Feng[2]*, Roman Fasel[1,5]*

[1]nanotech@surfaces laboratory, Empa – Swiss Federal Laboratories for Materials Science and Technology, Dübendorf, Switzerland

[2]Faculty of Chemistry and Food Chemistry & Center for Advancing Electronics Dresden, Technical University of Dresden, Dresden, Germany

[3]Department of Applied Physics, Aalto University, Aalto, Finland

[4]Department of Synthetic Chemistry, Max Planck Institute for Polymer Research, Mainz, Germany

[5]Department of Chemistry and Biochemistry, University of Bern, Bern, Switzerland

*E-mail: xinliang.feng@tu-dresden.de, roman.fasel@empa.ch

†These authors contributed equally to this work

The chemical versatility of carbon imparts manifold properties to organic compounds, wherein magnetism remains one of the most desirable but also elusive[1]. Polycyclic aromatic hydrocarbons, also referred to as nanographenes, show a critical dependence of electronic structure on the topologies of the edges and the π-electron network, which makes them model systems to engineer unconventional properties including magnetism. In 1972, Erich Clar envisioned a bowtie-shaped nanographene $C_{38}H_{18}$[2,3], where topological frustration in the π-electron network renders it impossible to assign a classical Kekulé structure without leaving unpaired electrons, driving the system into a magnetically non-trivial ground state[4]. Here, we report the experimental realisation and in-depth characterisation of this emblematic nanographene known as Clar's goblet. Scanning tunneling microscopy and spin excitation spectroscopy of individual molecules on a gold surface reveal a robust antiferromagnetic order with an exchange coupling of 23 meV, exceeding the Landauer limit of minimum energy dissipation at room temperature[5]. Through atomic manipulation, we realise switching of magnetic ground states in molecules with quenched spins. Our results provide direct evidence of carbon magnetism in a hitherto unrealised class of nanographenes[6], and prove a long-predicted paradigm where topological frustration entails unconventional magnetism, with implications for room-temperature carbon-based spintronics[7,8].

The current paradigm in carbon magnetism revolves around two concepts. The first concept involves nanographenes (NGs) and graphene nanoribbons (GNRs) with zigzag edge topologies, which are predicted to host low-energy edge-localised states. With increasing system size, these states approach the Fermi level, and Coulomb repulsion between valence electrons may trigger spin polarisation[9,10]. Although evidence of edge states in GNRs has been found[11,12], a firm proof of magnetism therein is lacking, and only recently, magnetic response in certain fused GNR junctions has been reported[13]. The second and conceptually simpler route involves inducing sublattice imbalance in the bipartite graphene lattice, which translates to a spin imbalance as per Lieb's theorem[14]. This scenario has been realised through creation of atomic defects that remove a p_z orbital[15–18], or in NGs with specific shapes[19] where sublattice imbalance is structurally inherent[20–24], such that it is impossible to assign a classical Kekulé structure (*i.e.* alternating single and double bonds) without leaving unpaired electrons. We refer to such non-Kekulé NGs as sublattice-imbalanced NGs (Fig. 1a, b), and their magnetic nature in solution has been elucidated through electron spin resonance[20,21] and thermochromism[25,26] studies. While presence of spin-split states in these systems has been detected in scanning tunneling microscopy and spectroscopy (STM/STS) measurements[22–24], direct magnetic response, however, has not been reported. Finally, ferromagnetism in twisted bilayer graphene has been recently discovered[27], which extends the repertoire of concepts in carbon magnetism.

Departing from the above notions, certain benzenoid topologies have long been hypothesised to result in non-Kekulé NGs despite the absence of sublattice imbalance[6]. This non-trivial feature is a consequence of topological frustration in the underlying π-electron network, which renders it impossible to concomitantly pair all p_z orbitals to form π-bonds, thus generating uncompensated radicals[4]. We refer to this class of NGs as topologically-frustrated NGs (TF-NGs, Fig. 1a, b). They can only be constructed for $h \geq 11$ (where h is the total number of hexagons in a NG), with graph-theoretical analysis having shown that TF-NGs constitute an exceedingly small fraction of the total number of NGs for a given h, with abundancies < 0.1%[6,28]. TF-NGs are predicted to exhibit large magnetic coupling strengths and magnetic state-dependent spatial distribution of frontier orbitals, with implications for spin logic devices and molecular switches[4,29,30]. However, their synthesis has never been achieved to date due to their high reactivity and lack of synthetic protocols.

The synthesis of Clar's goblet (**1**) involves precursor compound **2** (Fig. 1c), wherein the methyl groups connected to the central benzene ring serve as pre-selected reactive sites that are expected to undergo surface-catalysed oxidative ring closure against the anthracene moieties to form **1**. To reach the highly sterically-hindered precursor **2**, a multi-step organic synthesis was performed (see Supplementary Information). In particular, an intramolecular Friedel-Crafts-type cyclisation of the key intermediate compound **9** under Lewis acid conditions was employed to form the two flanking anthracenyl substituents on the six-fold substituted benzene core. **2** was obtained after silica column chromatography in 15% yield, and unambigu-

ously characterised *via* nuclear magnetic resonance spectroscopy and mass spectrometry. **2** was then sublimed on a Au(111) surface and annealed to 300 °C to promote on-surface reactions. The choice of Au(111) stems from its relative inertness compared to other coinage metal surfaces, which allows probing the intrinsic electronic properties of molecular adsorbates without significant perturbation. Figure 1d presents an overview STM image of the surface after the annealing step, showing individual molecules, and linearly- and irregularly-fused oligomers. High-resolution (HR) STM image of an individual molecule (Fig. 1e) reveals an overall uniform topography with five distinct lobes at the termini. To obtain the bond-resolved structure of the molecule, ultrahigh-resolution (UHR) STM imaging was conducted in the regime of tip-molecule Pauli repulsion[31,32] (see Methods), which confirms the successful formation of **1** (Fig. 1f, Supplementary Fig. 1).

To capture the fundamental electronic structure of **1**, we employ the nearest-neighbour tight-binding (TB) and mean-field Hubbard (MFH) models, which provide an appropriate balance between a clear understanding and relevant description of the low-energy electronic structure of NGs[1]. Concurrently, our results are supported by *ab-initio* calculations where relevant. The salient features in the TB energy spectrum of **1** are two zero-energy states populated by two electrons (Fig. 2a). To describe magnetism, electron-electron interactions are included through on-site Coulomb repulsion within the MFH model, which lifts the degeneracy of the zero-energy states *via* spin polarisation and opens an energy gap (Fig. 2b). The MFH solution predicts an antiferromagnetic (open-shell singlet) ground state of **1** (Fig. 2c), which is in agreement with previous theoretical reports[33–35] and our spin-polarised density functional theory (DFT) calculations, wherein for **1** both in the gas phase and on Au(111), the open-shell singlet state is the ground state, with the ferromagnetic (open-shell triplet) state 25.4 meV (gas phase) and 13.2 meV (on-surface) higher in energy (Supplementary Fig. 2). The spin-polarised wave functions of the singly occupied and unoccupied molecular orbitals (SOMOs and SUMOs) are spatially separated and sublattice-polarised (Fig. 2d). Figure 2e shows the spin density distribution of **1** and illustrates spin polarisation of the system – although the total spin $S = 0$, spin up and spin down population are sublattice-polarised and localised on opposite parts of **1**, thus maintaining a local spin polarisation.

The experimental electronic structure of **1** was characterised *via* dI/dV spectroscopy (Fig. 2f), where a series of reproducible features are found at -1.15 V (H-1), -300 mV (SO), +1.00 V (SU), +1.80 V (L+1) and +2.20 V (L+2). dI/dV maps recorded at the respective energies (Fig. 2g) exhibit excellent correspondence to the MFH local density of states (LDOS) maps of HOMO-1, SOMO, SUMO, LUMO+1 and LUMO+2 of **1** (Fig. 2h, HOMO/LUMO: highest occupied/lowest unoccupied molecular orbital), which confirms these spectroscopic features to be molecular orbital (MO) resonances. Detection of MOs with single occupation (*i.e.* SOMOs/SUMOs) exhibiting the same LDOS distribution in dI/dV maps implies spin splitting of the frontier orbitals, and therefore suggests a magnetic ground state of **1**. The experimental Coulomb gap of **1** is deduced to be 1.30 eV based on the energies of the SOMO and SUMO

resonances (Supplementary Fig. 3). For accurate theoretical assignment of the energies of MO resonances, we performed eigenvalue self-consistent GW calculations including screening effects from the underlying surface (GW+IC) for the open-shell singlet state of **1**. Figure 2i presents a comparative energy spectrum of the HOMO-1 to LUMO+1 resonances of **1** for GW+IC calculations and STS experiments, where both the GW+IC Coulomb gap and the relative energies of the charged excitations corresponding to HOMO-1 to LUMO+1 resonances match excellently with experimental values. Unambiguous evidence of magnetism in **1** is detected as low-energy spectral features in the vicinity of the Fermi level, in the form of steps located at ±23 mV (Fig. 2j, k). In contrast to resonant tunneling of electrons through MOs, which reflect as peaks in dI/dV spectroscopy, conductance steps symmetric around the Fermi energy indicate inelastic excitations. To visualise the spatial distribution of the excitation, we recorded dI/dV maps at ±23 mV (Fig. 2l), which agree well with the computed spin density distribution of **1** and resemble the SOMO/SUMO LDOS. Based on the S = 0 ground state of **1**, we ascribe these spectral features to singlet-triplet spin excitations[36] (S = 0 to S = 1, Fig. 2m), confirming a magnetic order in **1**. While the delocalised π-radical system of **1** confers the molecule with sufficient stability to prevent spin quenching upon adsorption on a metal, the broad and peaked profile of the excitation spectrum possibly indicates finite Kondo coupling of the individual spins with the surface[37].

The simple picture that emerges from the spectroscopic analyses of **1** is that of two spins that are exchange-coupled antiferromagnetically, with an effective exchange parameter J_{eff} = 23 meV. Therefore, increasing the separation of the spin-bearing moieties should lead to electronic decoupling of the spins, such that J_{eff} = 0 and the spins behave as free paramagnetic centres with S = ½. It is then plausible that screening of the individual spins by itinerant conduction electrons of the surface should result in a many-body Kondo ground state[38]. A straightforward route to confirm such a scenario is outlined in Fig. 3a, wherein linear fusion of **1** to generate a dimer (*di*-**1**) is envisaged, such that the spins are separated by a large non-magnetic unit. We find that such linearly-fused oligomers coexist with **1** (Fig. 1d) and constitute larger members of TF-NGs. Figure 3b shows the HR-STM image of *di*-**1**, where the termini retain the five-lobed appearance of **1** and no LDOS feature is seen at the central part. The corresponding UHR-STM image (Fig. 3c, d) clearly shows the bond-resolved structure of *di*-**1**, and importantly, reveals considerable accumulation of LDOS near zero bias at the termini – a feature absent in **1**. Accordingly, dI/dV spectroscopy reveals pronounced zero-bias peaks (ZBPs) that are localised at the terminal triangular motifs of *di*-**1**, and are notably absent at the central part (Fig. 3e). The resonance linewidth of the ZBPs exhibits an anomalous broadening with increasing temperature, and follows the characteristic trend of a Kondo-screened state with the Kondo temperature T_K = 37 ± 4 K (Fig. 3f, g). Furthermore, the ZBPs exhibit pronounced attenuation and eventual Zeeman splitting with increasing magnetic field (Fig. 3h, i), which unambiguously proves the ZBPs to be Kondo resonances (see Supplementary Note 5 for fit procedures). MFH-calculated singlet-triplet (ST) gaps of **1** and *di*-**1** support

our experimental observations, wherein over a wide range of the on-site Coulomb repulsion (U), the ST gap of **1** presents a finite value with a monotonic increase with increasing U, while that of *di*-**1** remains zero indicating no spin coupling (Extended Data Fig. 1). The computed spin density distribution of *di*-**1** (Fig. 3j) reveals negligible spin density at the central part of the molecule, in support of the spatial extent of Kondo resonance (Supplementary Fig. 4). Further spectroscopy data on *di*-**1** are reported in Supplementary Fig. 5 and 6.

The presence of unpaired spins renders **1** susceptible to spin quenching *via* site-specific chemisorption on Au(111). While **1** is mostly adsorbed on the *fcc* sites at high coverage, it is found pinned to the elbows of the herringbone ridges at low coverage (Supplementary Fig. 7, we refer to these species as **1′**), that are known to be reactive sites due to a lower atomic coordination. Figure 4a presents a HR-STM image of **1′**, which reveals a missing central lobe at the end bound to the elbow[39] (highlighted with an arrow). The corresponding UHR-STM image (Fig. 4b, Supplementary Fig. 8) shows two notable features: (i) a significant loss of resolution at the central hexagon apex of the end bound to the elbow, and (ii) pronounced accumulation of LDOS near zero bias at the unbound end – both features absent in **1**. This large LDOS manifests as ZBPs at the unbound end, which exhibit temperature-dependent characteristics of a Kondo resonance (Extended Data Fig. 2). Since the external carbon atom of the terminal central hexagon in **1** hosts the largest spin density (Fig. 2e), we speculate that bonding to an under-coordinated gold atom at the elbow quenches the spin at that site, such that **1′**, whose chemical structure is proposed in Fig. 4c, can be described as an effective spin-½ system. To model this scenario, we consider the DFT-computed structure shown in Fig. 4d, wherein a gold atom is chemisorbed to **1** at one of its ends. First, it is seen that the carbon atom bound to the gold atom (indicated by an arrow) shows a slight out-of-plane displacement toward the gold atom, explaining the corresponding loss of resolution in the UHR-STM image. Second, the computed spin density distribution of **1′** reveals complete quenching of magnetic moment at the bound end, with spin localisation only at the unperturbed end (*i.e.* a spin-½ system), in agreement with the experimental Kondo map (Supplementary Fig. 4). To confirm our assumption we performed lateral manipulation of **1′**. As **1′** is manipulated away from the elbow site, a noticeable change in topography (Fig. 4e, g) accompanies recovery of spin excitations (Fig. 4f, h), indicating a $S = ½$ to $S = 0$ switching of the magnetic ground state. Additional spectroscopy measurements on **1′** are reported in Supplementary Fig. 9. We also find species on the surface where the central carbon atom at one end is passivated by two hydrogen atoms (**2H-1**, Fig. 4c). Figure 4i shows a **1** (left) and **2H-1** (right) molecule, where the upper end of **2H-1** exhibits a featureless appearance due to the central carbon atom saturated with two hydrogen atoms. Contrary to **1**, which exhibits spin excitations at both ends, we find a featureless dI/dV signal at the upper end of **2H-1** and a pronounced ZBP at the lower (pristine) end (Fig. 4j). Conceptually, this is the same scenario as in **1′**, where the spin density at the upper end is quenched *via* bonding to two hydrogen atoms (Supplementary Fig. 2), while the surviving spin-½ at the lower end is screened by the surface electrons, associating the ZBP to a

Kondo resonance. Dissociation of the extra hydrogen atom in **2H-1** through a voltage pulse results in the formation of **1** (Fig. 4k) and leads to recovery of spin excitations (Fig. 4l).

We have demonstrated magnetism in Clar's goblet, a member of the elusive class of TF-NGs. The antiferromagnetic ground state, which survives contact with a metal electrode, is distinguished by an exchange coupling strength of 23 meV that surpasses those of transition metal nanomagnets[36] and exceeds the Landauer limit of minimum energy dissipation, $k_BT\ln(2) \approx 18$ meV, at $T = 300$ K[5] – raising hopes for fault-tolerant spin logic operations near room temperature[7]. Our studies provide a firm basis for investigation of larger members of TF-NGs that are predicted to exhibit magnetic coupling strengths well beyond the thermodynamic threshold[4], thereby ushering in carbon-based spintronics.

References

1. Yazyev, O. V. Emergence of magnetism in graphene materials and nanostructures. *Rep. Prog. Phys.* **73,** 056501 (2010).

2. Clar, E., *The Aromatic Sextet* (Wiley, New York, 1972).

3. Clar, E. & Mackay, C. C. Circobiphenyl and the attempted synthesis of 1:14, 3:4, 7:8, 10:11-tetrabenzoperopyrene. *Tetrahedron* **28,** 6041–6047 (1972).

4. Wang, W. L., Yazyev, O. V., Meng, S. & Kaxiras, E. Topological Frustration in Graphene Nanoflakes: Magnetic Order and Spin Logic Devices. *Phys. Rev. Lett.* **102,** 157201 (2009).

5. Landauer, R. Irreversibility and Heat Generation in the Computing Process. *IBM J. Res. Dev.* **5,** 183–191 (1961).

6. Cyvin, S. J., Brunvoll, J. & Cyvin, B. N. The hunt for concealed non-Kekuléan polyhexes. *J. Math. Chem.* **4,** 47–54 (1990).

7. Agarwal, H., Pramanik, S. & Bandyopadhyay, S. Single spin universal Boolean logic gate. *New J. Phys.* **10,** 015001 (2008).

8. Han, W., Kawakami, R. K., Gmitra, M. & Fabian, J. Graphene spintronics. *Nat. Nanotechnol.* **9,** 794–807 (2014).

9. Nakada, K., Fujita, M., Dresselhaus, G. & Dresselhaus, M. S. Edge state in graphene ribbons: Nanometer size effect and edge shape dependence. *Phys. Rev. B* **54,** 17954–17961 (1996).

10. Fernández-Rossier, J. & Palacios, J. J. Magnetism in Graphene Nanoislands. *Phys. Rev. Lett.* **99,** 177204 (2007).

11. Tao, C. *et al.* Spatially resolving edge states of chiral graphene nanoribbons. *Nat. Phys.* **7,** 616–620 (2011).

12. Ruffieux, P. *et al.* On-surface synthesis of graphene nanoribbons with zigzag edge topology. *Nature* **531,** 489–492 (2016).

13. Li, J. *et al.* Single spin localization and manipulation in graphene open-shell nanostructures. *Nat. Commun.* **10,** 200 (2019).

14. Lieb, E. H. Two Theorems on the Hubbard Model. *Phys. Rev. Lett.* **62,** 1201–1204 (1989).

15. Ugeda, M. M., Brihuega, I., Guinea, F. & Gómez-Rodríguez, J. M. Missing Atom as a Source of Carbon Magnetism. *Phys. Rev. Lett.* **104,** 096804 (2010).

16. Nair, R. R. *et al.* Spin-half paramagnetism in graphene induced by point defects. *Nat. Phys.* **8,** 199–202 (2012).

17. Zhang, Y. *et al.* Scanning Tunneling Microscopy of the π Magnetism of a Single Carbon Vacancy in Graphene. *Phys. Rev. Lett.* **117,** 166801 (2016).

18. González-Herrero, H. *et al.* Atomic-scale control of graphene magnetism by using hydrogen atoms. *Science* **352,** 437–441 (2016).

19. Morita, Y., Suzuki, S., Sato, K. & Takui, T. Synthetic organic spin chemistry for structurally well-defined open-shell graphene fragments. *Nat. Chem.* **3,** 197–204 (2011).

20. Goto, K. *et al.* A Stable Neutral Hydrocarbon Radical: Synthesis, Crystal Structure, and Physical Properties of 2,5,8-Tri-*tert*-butyl-phenalenyl. *J. Am. Chem. Soc.* **121,** 1619–1620 (1999).

21. Inoue, J. *et al.* The First Detection of a Clar's Hydrocarbon, 2,6,10-Tri-*tert*-Butyltriangulene: A Ground-State Triplet of Non-Kekulé Polynuclear Benzenoid Hydrocarbon. *J. Am. Chem. Soc.* **123,** 12702–12703 (2001).

22. Pavliček, N. *et al.* Synthesis and characterization of triangulene. *Nat. Nanotechnol.* **12,** 308–311 (2017).

23. Mishra, S. *et al.* Synthesis and Characterization of π-Extended Triangulene. *J. Am. Chem. Soc.* **141,** 10621–10625 (2019).

24. Su, J. *et al.* Atomically precise bottom-up synthesis of π-extended [5]triangulene. *Sci. Adv.* **5,** eaav7717 (2019).

25. Small, D. *et al.* Intermolecular π-to-π Bonding between Stacked Aromatic Dyads. Experimental and Theoretical Binding Energies and Near-IR Optical Transitions for Phenalenyl Radical/Radical versus Radical/Cation Dimerizations. *J. Am. Chem. Soc.* **126,** 13850–13858 (2004).

26. Suzuki, S. *et al.* Aromaticity on the Pancake-Bonded Dimer of Neutral Phenalenyl Radical as Studied by MS and NMR Spectroscopies and NICS Analysis. *J. Am. Chem. Soc.* **128,** 2530–2531 (2006).

27. Sharpe, A. L. *et al.* Emergent ferromagnetism near three-quarters filling in twisted bilayer graphene. *Science* **365,** 605–608 (2019).

28. Cyvin, B. N., Brunvoll, J. & Cyvin, S. J. Enumeration of benzenoid systems and other polyhexes. in *Advances in the Theory of Benzenoid Hydrocarbons II* (ed. Gutman, I.) 65–180 (Springer, Berlin, Heidelberg, 1992).

29. Kang, J., Wu, F. & Li, J. Spin filter and molecular switch based on bowtie-shaped graphene nanoflake. *J. Appl. Phys.* **112,** 104328 (2012).

30. Zhou, A., Sheng, W. & Xu, S. J. Electric field driven magnetic phase transition in graphene nanoflakes. *Appl. Phys. Lett.* **103,** 133103 (2013).

31. Temirov, R., Soubatch, S., Neucheva, O., Lassise, A. C. & Tautz, F. S. A novel method achieving ultra-high geometrical resolution in scanning tunnelling microscopy. *New J. Phys.* **10,** 053012 (2008).

32. Gross, L., Mohn, F., Moll, N., Liljeroth, P. & Meyer, G. The Chemical Structure of a Molecule Resolved by Atomic Force Microscopy. *Science* **325,** 1110–1114 (2009).

33. Pogodin, S. & Agranat, I. Clar Goblet and Related Non-Kekulé Benzenoid LPAHs. A Theoretical Study. *J. Org. Chem.* **68,** 2720–2727 (2003).

34. Das, A., Müller, T., Plasser, F. & Lischka, H. Polyradical Character of Triangular Non-Kekulé Structures, Zethrenes, *p*-Quinodimethane-Linked Bisphenalenyl, and the Clar Goblet in Comparison: An Extended Multireference Study. *J. Phys. Chem. A* **120,** 1625–1636 (2016).

35. Ortiz, R. *et al.* Exchange Rules for Diradical π-Conjugated Hydrocarbons. *Nano Lett.* **19,** 5991–5997 (2019).

36. Hirjibehedin, C. F., Lutz, C. P. & Heinrich, A. J. Spin Coupling in Engineered Atomic Structures. *Science* **312,** 1021–1024 (2006).

37. Ternes, M. Spin excitations and correlations in scanning tunneling spectroscopy. *New J. Phys.* **17,** 063016 (2015).

38. Ternes, M., Heinrich, A. J. & Schneider, W.-D. Spectroscopic manifestations of the Kondo effect on single adatoms. *J. Phys. Condens. Matter* **21,** 053001 (2008).

39. van der Lit, J. *et al.* Suppression of electron–vibron coupling in graphene nanoribbons contacted via a single atom. *Nat. Commun.* **4,** 2023 (2013).

Acknowledgments

We thank Md Nurul Huda for assistance with STM measurements, Tilo Lübken for assistance with NMR measurements, and Ricardo Ortiz, Joaquin Fernández-Rossier and Daniele Passerone for stimulating discussions. This work was supported by the Swiss National Science Foundation (grant number 200020-182015 and IZLCZ2-170184), the NCCR MARVEL funded by the Swiss National Science Foundation (grant number 51NF40-182892), the European Union's Horizon 2020 research and innovation program under grant agreement numbers 696656 and 785219 (Graphene Flagship Core 2), the Office of Naval Research (N00014-18-1-2708), ERC Consolidator grant (T2DCP, number 819698), the German Research Foundation (DFG) within the Cluster of Excellence Center for Advancing Electronics Dresden (cfaed) and EnhanceNano (number 391979941), and the European Social Fund and the Federal State of Saxony (ESF-Project GRAPHD, TU Dresden). Computational support from the Swiss Supercomputing Center (CSCS) under project ID s904 is gratefully acknowledged. S.K. and P.L acknowledge funding from the Academy of Finland (grant numbers 309975 and 318995) and the European Research Council (ERC-AdG number 788185), and the facilities of the Aalto Nanomicroscopy Centre.

Author contributions

K.M., X.F., P.R and R.F. conceived the project. D.B. and R.B. synthesised and characterised the precursor molecules. S.M. performed the on-surface synthesis and STM experiments. S.M. and S.K. performed the magnetic field STM experiments under the supervision of P.L. S.M. and O.G. performed tight-binding calculations. K.E. performed DFT and GW calculations under the supervision of C.A.P. The manuscript was written by S.M., with contributions from all co-authors.

Additional information

Supplementary information is available in the online version of the paper. Reprints and permission information is available online at www.nature.com/reprints. Correspondence and requests for materials should be addressed to X.F. or R.F.

Competing financial interests

The authors declare no competing interests.

Figure captions

Figure 1 | Synthesis and structural characterisation of Clar's goblet. a, Conceptual routes towards magnetism in graphene and NGs. **b,** Schematic illustrating the difference between a sublattice-imbalanced NG (top) and a topologically-frustrated NG (bottom) in terms of sublattice imbalance and resulting total spin from Lieb's theorem. Filled and empty circles represent *A* and *B* sublattice atoms, respectively. **c,** Combined in-solution and on-surface synthetic route towards **1**. **d,** Overview STM image after annealing **2** on Au(111) at 300 °C, revealing individual molecules (one of them is highlighted with a square) coexisting with linear (highlighted with arrows) and branched oligomers (V = -30 mV, I = 150 pA). **e,** HR-STM image of **1** acquired with a CO-functionalised tip (V = -100 mV, I = 100 pA). **f,** Corresponding Laplace-filtered UHR-STM image showing the bond-resolved structure of **1** (V = -5 mV, I = 50 pA, Δz = -0.95 Å). Scale bars: 5 nm **(d)**, 0.5 nm **(e, f)**.

Figure 2 | Electronic and magnetic characterisation of Clar's goblet. a, b, Nearest-neighbor TB **(a)** and MFH **(b)** energy spectrum of **1**. **c,** Schematic representation of frontier states. $\Psi_{L,\uparrow/\downarrow}$ and $\Psi_{R,\uparrow/\downarrow}$ indicate spin-polarised wave functions localised on the left and right sides of **1**, respectively. **d,** Calculated wave functions of SOMOs. Red/green isosurfaces denote opposite signs of wave function. **e,** MFH spin density distribution of **1**. Blue/red isosurfaces denote spin up/spin down density. **f,** dI/dV spectra acquired on **1** (V = -2 V, I = 300 pA, V_{rms} = 16 mV). Labels correspond to orbital resonances as explained in the text. Inset: HR-STM image of **1**. **g,** dI/dV maps acquired at the peaks/regions labeled H-1, SO, SU, L+1 and L+2 in **(f)**. **h,** MFH-LDOS maps of the HOMO-1, SOMO, SUMO, LUMO+1 and LUMO+2 of **1**. **i,** Energies of the HOMO-1 to LUMO+1 orbital resonances of **1** on Au(111) shown for GW+IC calculations and STS experiments, with corresponding Coulomb gaps indicated in red. Energies of the calculated and experimental levels are aligned at HOMO-1. **j, k,** dI/dV (**(j)**, V = -50 mV, I = 500 pA, V_{rms} = 400 μV) and d^2I/dV^2 (**(k)**, V = -50 mV, I = 1.5 nA, V_{rms} =

4 mV) spectrum acquired on **1** in the vicinity of the Fermi level revealing inelastic spin excitation at ±23 mV. **l,** dI/dV maps acquired at ±23 mV. **m,** Schematic representation of the spin excitation. Tip positions for spectra shown in **(f, j, k)** are marked by filled circles in **(f)**. All dI/dV spectra shown in individual panels herein and in rest of the figures are vertically offset for visual clarity. For the dI/dV maps, I = 250 pA–350 pA, with V_{rms} = 22 mV **(g)** and 10 mV **(l)**. The scale bar of 0.5 nm in the inset of **(f)** also applies to **(g, h, l)**.

Figure 3 | Spin decoupling in a fused dimer. a, Schematic representation of the formation of *di*-**1** *via* linear fusion of **1**. Grey filled parts highlight spin-bearing moieties. **b,** HR-STM image of *di*-**1** acquired with a CO-functionalised tip (V = -100 mV, I = 50 pA). **c, d,** Corresponding UHR-STM image of *di*-**1 (c)** and its Laplace transform **(d)** showing large LDOS accumulation at the termini (V = -5 mV, I = 50 pA, Δz = -0.40 Å). **e,** dI/dV spectra acquired in the vicinity of the Fermi level revealing Kondo resonances localised at the terminal triangular motifs of *di*-**1** (tip positions are marked by filled circles in **(c)**). **f,** Temperature evolution of the Kondo resonance with fit to the experimental data with Frota function. **g,** Extracted half width at half maximum (HWHM) of the Kondo resonance as a function of temperature, with corresponding fit using Fermi-liquid model. **h,** Magnetic field evolution of the Kondo resonance at T = 1.6 K with corresponding fit with Frota function. A Zeeman splitting is clearly resolved at 10 T as indicated by two arrows. **i,** Extracted Zeeman splitting of the Kondo resonance as a function of magnetic field with corresponding linear fit. The extracted Landé factor g = 2.3 ± 0.2 from the fit is close to the value for a free electron, g_0 = 2. **j,** MFH spin density distribution of *di*-**1**. Open feedback parameters for dI/dV spectra: V = -20 mV, I = 300 pA, V_{rms} = 400 μV **(e, f)** and V = -20 mV, I = 1 nA, V_{mod} = 200 μV **(h)**. Scale bars: 0.5 nm.

Figure 4 | Spin quenching and switching of magnetic ground states in 1′ and 2H-1. a, HR-STM image of **1′** acquired with a CO-functionalised tip (V = -400 mV, I = 50 pA). The arrow highlights a missing central lobe at the end bound to the elbow. **b,** Corresponding UHR-STM image revealing considerable LDOS accumulation at the unbound end and loss of resolution at the central hexagon apex of the bound end, as indicated with an arrow (V = -5 mV, I = 50 pA, Δz = -1.00 Å). **c,** Schematic representations of **1**, **1′** and **2H-1**. **d,** DFT-calculated spin density distribution of **1** chemisorbed to a gold atom (isovalue: ±0.003 a.u., left panel); and the magnified side view of the system, with the carbon atom bound to the gold atom indicated by an arrow (right panel). Carbon, hydrogen and gold atoms are coloured grey, white and yellow, respectively. **e, f,** STM image of **1′** **(e)**, V = -100 mV, I = 150 pA), and corresponding dI/dV spectra showing Kondo resonance at the unbound end **(f)**. **g, h,** STM image after lateral manipulation of **1′** to create **1** **(g)**, V = -100 mV, I = 100 pA), and dI/dV spectra showing recovery of spin excitations **(h)**. **i,** STM image of a **1** and **2H-1** molecule (V = -30 mV, I = 300 pA). **j,** dI/dV spectra showing Kondo resonance at the pristine end and a featureless signal at the dihydrogenated end of **2H-1**. **k, l,** STM image after voltage pulse-induced manipulation of **2H-1** to create **1** **(k)**, V = -30 mV, I = 300 pA), and dI/dV spectra demonstrating recovery of spin excitations **(l)**. Tip positions for spectra shown in **(f, h, j, l)** are

marked by filled circles in **(e, g, i, k)**, respectively. Open feedback parameters for dI/dV spectra: V = -50 mV, I = 500 pA, V_{rms} = 400 μV. Scale bars: 0.5 nm **(a, b)**, 1 nm **(e, g, i, k)**.

Methods

Synthesis of molecular precursor: The detailed chemical synthesis of molecular precursor **2** along with solution characterisation data is reported in Supplementary Information (Supplementary Schemes 1-8 and Supplementary Figures 10-35).

Sample preparation and STM/STS measurements. STM measurements were performed with two commercial low-temperature systems operating at base pressures below 1×10^{-10} mbar: a Scienta Omicron LT-STM operating at 4.5 K, and a Unisoku USM-1300 STM operating at 1.6 K with a maximum out-of-plane magnetic field of 11 T. Au(111) single crystal surfaces were prepared by iterative cycles of Ar^+ sputtering and subsequent annealing to 450 °C. The surface quality was ensured through STM imaging before deposition of precursor molecules. Precursor **2** was contained in a quartz crucible and sublimed from a home-built evaporator at 180 °C onto Au(111) surface held at room temperature. STM images and dI/dV maps were recorded in constant-current mode. Unless noted otherwise, STM imaging and spectroscopy were conducted with metallic (*i.e.* gold-coated tungsten) tips which provided reproducible spectroscopic signatures of the Au(111) surface state on the bare surface. Tunneling bias voltages are given with respect to the sample. dI/dV and d^2I/dV^2 spectra, and dI/dV maps were obtained with a lock-in amplifier (f = 860 Hz), wherein a signal proportional to dI/dV (d^2I/dV^2) was obtained from the first (second) harmonic of the tunneling current. Lock-in modulation voltages for individual measurements are provided in the respective figure captions, wherein V_{mod} and V_{rms} refer to the peak-to-peak and root mean square values of the modulation amplitude. UHR-STM images were acquired by recording the current channel while scanning the molecules in constant-height mode with CO-functionalised tips. Open feedback parameters and subsequent tip approach distance (*i.e.* Δz) for each image are indicated in the figure captions. CO molecules (for tip preparation) were deposited on a cold sample (T < 13 K) containing bilayer NaCl(001) islands. To conduct voltage pulse-induced manipulation, we first positioned the STM tip at the centre of the molecule at V = 100 mV and I = 2 pA and switched off the feedback loop. The tip was subsequently retracted by ~ 5 Å to limit the tunneling current to a few pA. Finally, the tunneling bias was gradually increased until an abrupt change in the tunneling current was observed, corresponding to a manipulation event. In our experiments, we achieved reproducible manipulation in a bias range of 3.7-4.0 V, which is consistent with the dissociation of a H atom from a $–CH_2$ group observed in previous reports[22]. STM lateral manipulation was conducted by moving the tip along a defined trajectory over the molecule at $V \leq 100$ mV and $I \geq 5$ nA. All data shown in this study were acquired at a sample temperature of 4.5 K, unless otherwise stated. The data were analyzed and processed with Wavemetrics Igor Pro or WSxM[40] software.

Tight-binding calculations of electronic structure. The tight-binding calculations of the molecular π-electron systems have been performed by numerically solving the Mean-Field-Hubbard Hamiltonian with first nearest-neighbour hopping:

$$\widehat{H}_{MFH} = -t \sum_{\langle\alpha,\beta\rangle,\sigma} c^{\dagger}_{\alpha,\sigma}\, c^{-}_{\beta,\sigma} + U \sum_{\alpha,\sigma} \langle n_{\alpha,\sigma}\rangle n_{\alpha,\bar{\sigma}} - U \sum_{\alpha} \langle n_{\alpha,\uparrow}\rangle \langle n_{\alpha,\downarrow}\rangle \qquad (1)$$

Here, $c^{\dagger}_{\alpha,\sigma}$ and $c^{-}_{\beta,\sigma}$ denote the spin selective ($\sigma \in \{\uparrow,\downarrow\}$) creation and annihilation operator at neighbouring sites α and β, t the nearest-neighbour hopping parameter (with t = 2.7 eV used here), U the on-site Hubbard parameter, $n_{\alpha,\sigma}$ the number operator and $\langle n_{\alpha,\sigma}\rangle$ the mean occupation number at site α. Orbital electron densities of the nth-eigenstate with energy E_n have been simulated from the corresponding state vector $a_{n,i,\sigma}$ by:

$$\rho_{n,\sigma}(\vec{r}) = \left| \sum_{i} a_{n,i,\sigma} \phi_{2p_z}(\vec{r} - \vec{r}_i) \right|^2 \qquad (2)$$

where i denotes the atomic site index, and ϕ_{2p_z} denotes the Slater $2p_z$ orbital for carbon (Z = 6).

DFT and GW calculations of electronic structure. To compute the adsorption geometry of the molecule on Au(111) surface at the DFT level of theory, we used the CP2K code[41,42]. We used periodic boundary conditions and the repeated slab scheme[43] to simulate the Au slab. A unit cell of 41.27×40.85 Å^2 (in the directions parallel to the surface) was used. The simulation cell contained four layers of Au and an additional layer of H atoms needed to passivate one side of the slab. In the [111] direction, we added 40Å of vacuum to decouple the system from its periodic replicas. To obtain the equilibrium geometries, we optimised the positions of the atoms belonging to the molecule, and to the two outermost layers of gold. A convergence criteria of 0.005 eV/Å was imposed on the atomic forces. We used Gaussian basis sets[44] for the representation of the electronic states (TZV2P for C and H and DZVP for Au). For the plane wave basis set used in CP2K to represent the charge density in Fourier space, we selected a cutoff of 600 Ry. We used norm-conserving pseudopotentials in the form proposed by Goedecker, Teter and Hutter[45]. We used the PBE parameterisation for the generalised gradient approximation of the exchange correlation functional[46]. To include van der Waals interactions in our simulations, we used the scheme proposed by Grimme[47]. The gas phase geometry optimisation and energy calculations for the restricted and unrestricted DFT were performed with a cell of $28 \times 28 \times 28$ Å^3, while other inputs were kept equivalent to the slab calculation. CP2K code was also used to perform the eigenvalue-self consistent GW calculations on the isolated molecular geometry corresponding to the adsorption conformation. For **1**, the calculation was performed based on the unrestricted DFT PBE wave functions of the open-shell singlet state. The unrestricted DFT-based GW energies of the spin up and spin down channels of **1** match within 20 meV. The shown energy levels for calculations correspond to the average of spin up and spin down channels for each orbital. We employed the GTH pseudopotentials

and analytic continuation with a two-pole model. The aug-DZVP basis set from Wilhelm *et al*.[48] was used. To account for screening by the metal surface, we applied the image charge model[49]. To determine the image plane position with respect to the molecular geometry, we used a distance of 1.42 Å between the image plane and the first surface layer, as reported by Kharche *et al*.[50] The calculations were performed *via* workflows based on the AiiDA platform[51].

Data availability. The data that support the findings of this study are available from the corresponding authors on reasonable request.

Code availability. The tight-binding calculations were performed using a custom-made code on the WaveMetrics Igor Pro platform. Details of the tight-binding code can be obtained from the corresponding authors on reasonable request.

References

40. Horcas, I. *et al.* WSXM: A software for scanning probe microscopy and a tool for nanotechnology. *Rev. Sci. Instrum.* **78,** 013705 (2007).

41. Hutter, J., Iannuzzi, M., Schiffmann, F. & Vandevondele, J. CP2K: atomistic simulations of condensed matter systems. *Wiley Interdiscip. Rev. Comput. Mol. Sci.* **4,** 15–25 (2014).

42. VandeVondele, J. *et al.* QUICKSTEP: Fast and accurate density functional calculations using a mixed Gaussian and plane waves approach. *Comput. Phys. Commun.* **167,** 103–128 (2005).

43. Pickett, W. E. Pseudopotential methods in condensed matter applications. *Comput. Phys. Rep.* **9,** 115–197 (1989).

44. VandeVondele, J. & Hutter, J. Gaussian basis sets for accurate calculations on molecular systems in gas and condensed phases. *J. Chem. Phys.* **127,** 114105 (2007).

45. Goedecker, S., Teter, M. & Hutter, J. Separable dual-space Gaussian pseudopotentials. *Phys. Rev. B* **54,** 1703–1710 (1996).

46. Lee, C.-C., Yamada-Takamura, Y. & Ozaki, T. Unfolding method for first-principles LCAO electronic structure calculations. *J. Phys. Condens. Matter* **25,** 345501 (2013).

47. Grimme, S., Antony, J., Ehrlich, S. & Krieg, H. A consistent and accurate *ab initio* parametrization of density functional dispersion correction (DFT-D) for the 94 elements H-Pu. *J. Chem. Phys.* **132,** 154104 (2010).

48. Wilhelm, J., Del Ben, M. & Hutter, J. GW in the Gaussian and Plane Waves Scheme with Application to Linear Acenes. *J. Chem. Theory Comput.* **12,** 3623–3635 (2016).

49. Neaton, J. B., Hybertsen, M. S. & Louie, S. G. Renormalization of Molecular Electronic Levels at Metal-Molecule Interfaces. *Phys. Rev. Lett.* **97,** 216405 (2006).

50. Kharche, N. & Meunier, V. Width and Crystal Orientation Dependent Band Gap Renormalization in Substrate-Supported Graphene Nanoribbons. *J. Phys. Chem. Lett.* **7,** 1526–1533 (2016).

51. Pizzi, G., Cepellotti, A., Sabatini, R., Marzari, N. & Kozinsky, B. AiiDA: automated interactive infrastructure and database for computational science. *Comput. Mater. Sci.* **111,** 218–230 (2016).

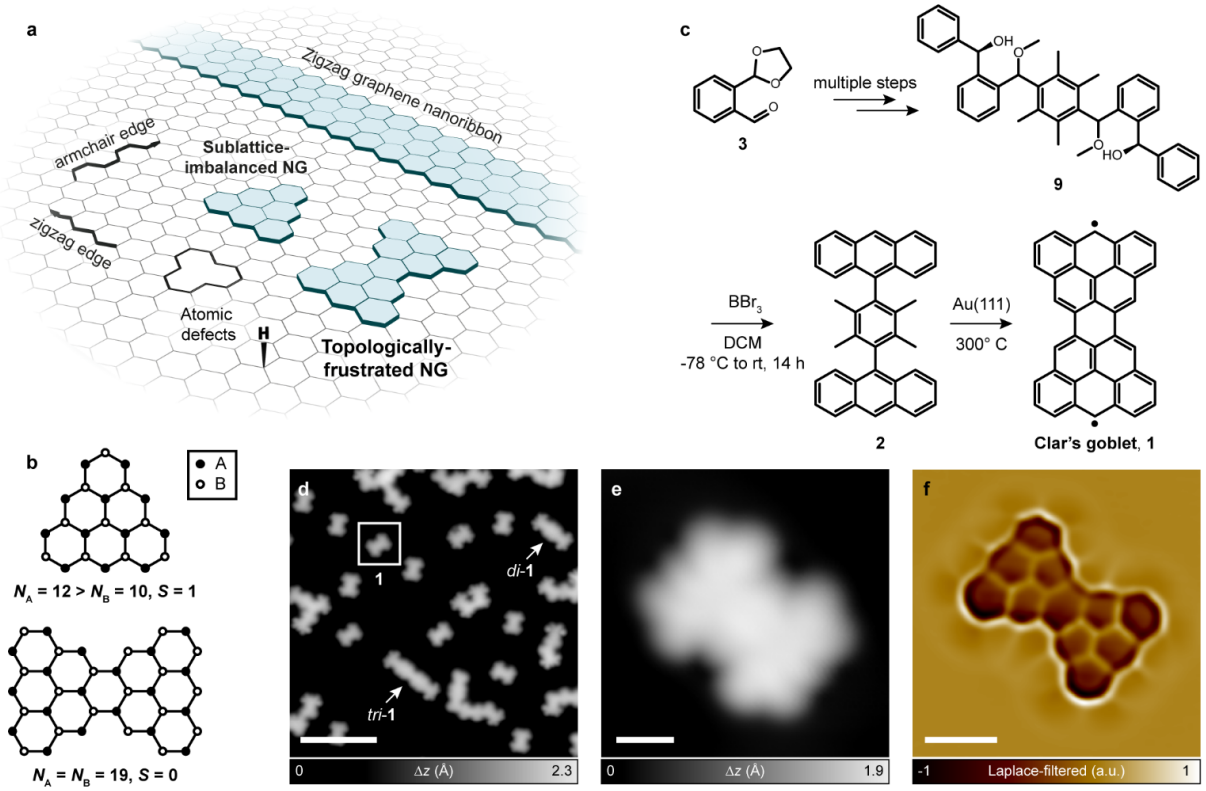
a
Zigzag graphene nanoribbon
armchair edge
Sublattice-imbalanced NG
zigzag edge
Atomic defects
H
Topologically-frustrated NG
c
3
multiple steps
9
BBr3
DCM
-78 °C to rt, 14 h
2
Au(111)
300° C
Clar's goblet, 1
b
A
B
NA = 12 > NB = 10, S = 1
NA = NB = 19, S = 0
d
1
di-1
tri-1
0
Δz (Å)
2.3
e
0
Δz (Å)
1.9
f
-1
Laplace-filtered (a.u.)
1

Figure 1

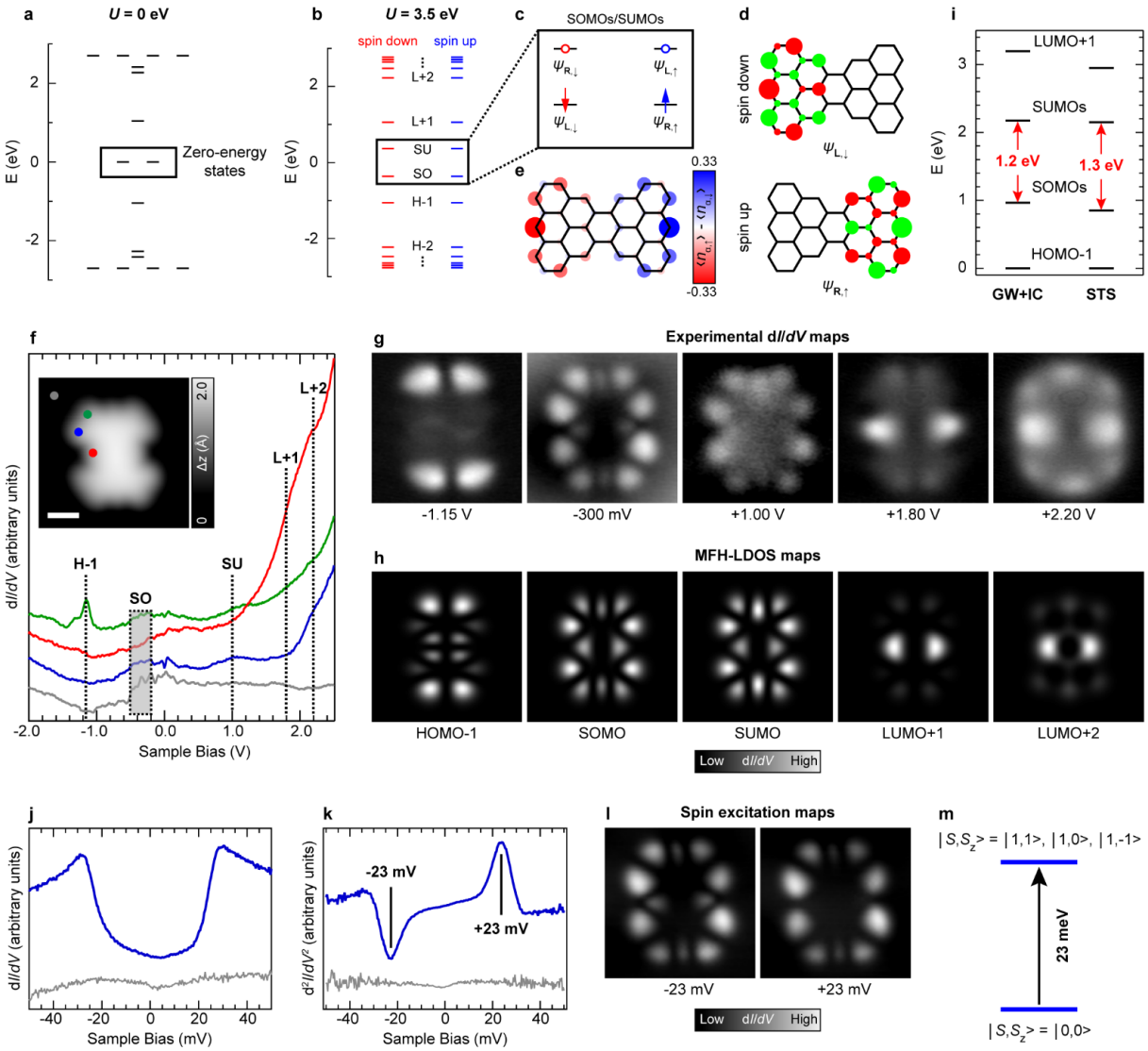
a
U = 0 eV
E (eV)
Zero-energy states
b
U = 3.5 eV
spin down
spin up
L+2
L+1
SU
SO
H-1
H-2
c
SOMOs/SUMOs
e
0.33
-0.33
d
spin down
spin up
i
LUMO+1
SUMOs
1.2 eV
1.3 eV
SOMOs
HOMO-1
GW+IC
STS
f
Δz (Å)
2.0
0
L+2
L+1
H-1
SO
SU
dI/dV (arbitrary units)
Sample Bias (V)
g
Experimental dI/dV maps
-1.15 V
-300 mV
+1.00 V
+1.80 V
+2.20 V
h
MFH-LDOS maps
HOMO-1
SOMO
SUMO
LUMO+1
LUMO+2
Low dI/dV High
j
dI/dV (arbitrary units)
Sample Bias (mV)
k
-23 mV
+23 mV
d²I/dV² (arbitrary units)
Sample Bias (mV)
l
Spin excitation maps
-23 mV
+23 mV
Low dI/dV High
m
|S,Sz> = |1,1>, |1,0>, |1,-1>
23 meV
|S,Sz> = |0,0>

Figure 2

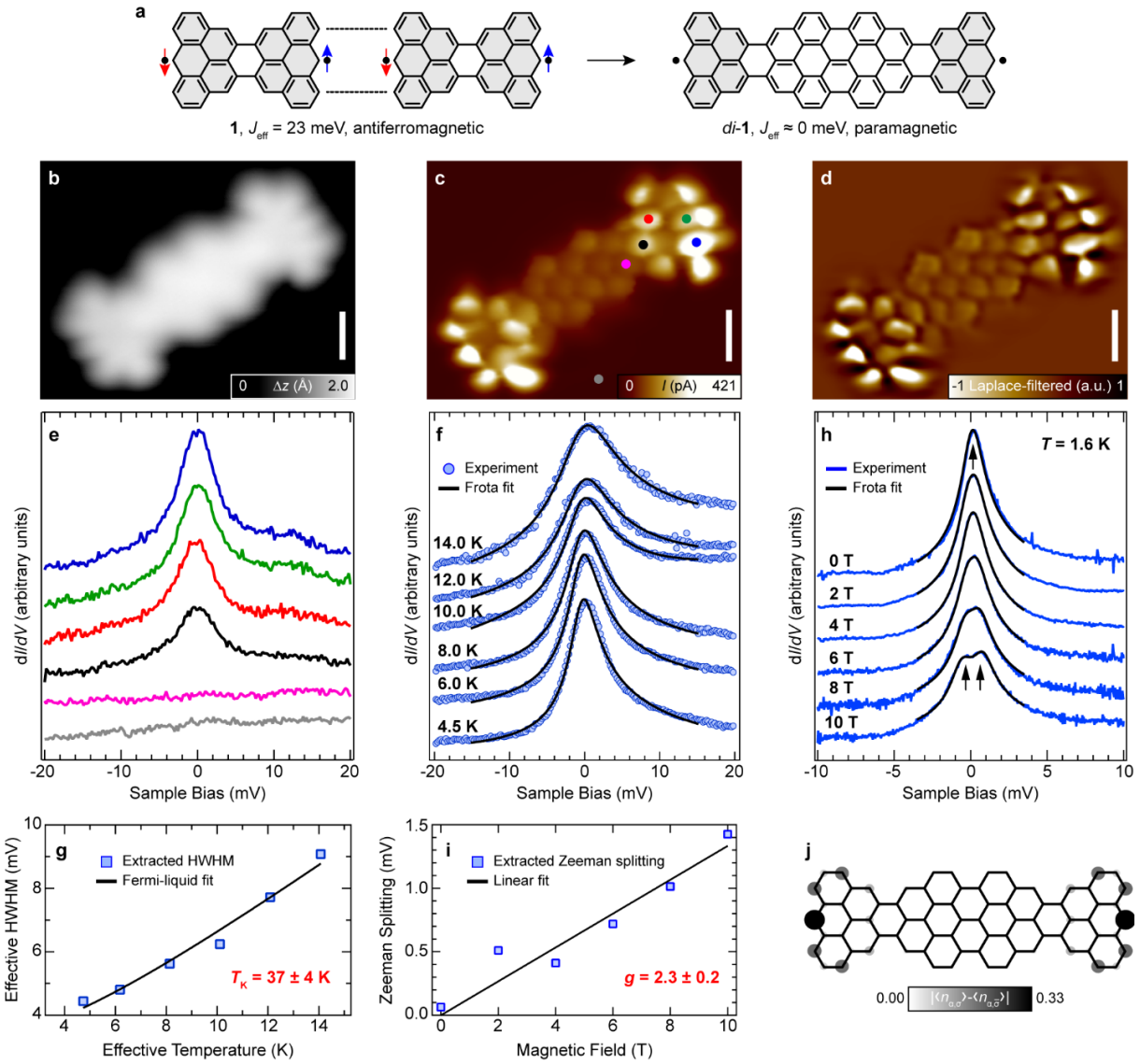
a
1, J_{eff} = 23 meV, antiferromagnetic
di-1, J_{eff} ≈ 0 meV, paramagnetic
b
0 Δz (Å) 2.0
c
0 I (pA) 421
d
-1 Laplace-filtered (a.u.) 1
e
dI/dV (arbitrary units)
Sample Bias (mV)
f
Experiment
Frota fit
14.0 K
12.0 K
10.0 K
8.0 K
6.0 K
4.5 K
dI/dV (arbitrary units)
Sample Bias (mV)
h
T = 1.6 K
Experiment
Frota fit
0 T
2 T
4 T
6 T
8 T
10 T
dI/dV (arbitrary units)
Sample Bias (mV)
g
Extracted HWHM
Fermi-liquid fit
T_K = 37 ± 4 K
Effective HWHM (mV)
Effective Temperature (K)
i
Extracted Zeeman splitting
Linear fit
g = 2.3 ± 0.2
Zeeman Splitting (mV)
Magnetic Field (T)
j
0.00
$|\langle n_{\alpha\sigma}\rangle - \langle n_{\bar{\alpha}\bar{\sigma}}\rangle|$
0.33

Figure 3

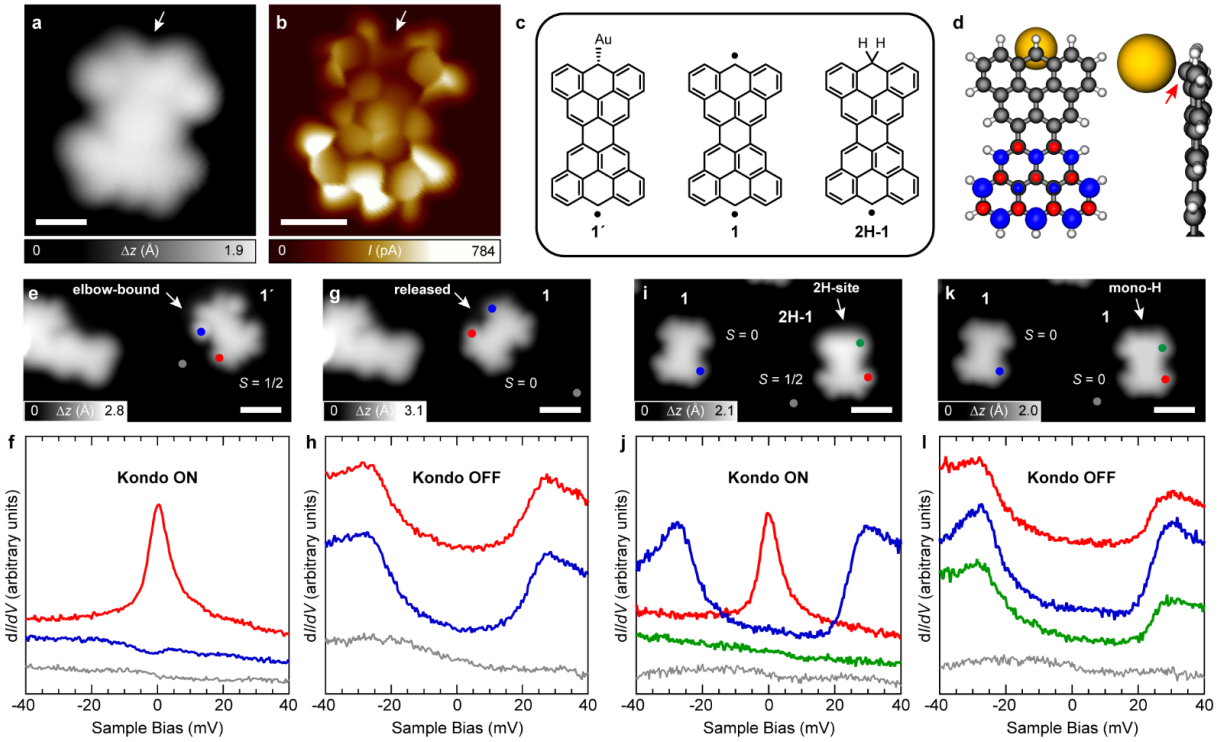
a
b
c
d
Au
H H
1´
1
2H-1
0 Δz (Å) 1.9
0 I (pA) 784
e elbow-bound
1´
S = 1/2
0 Δz (Å) 2.8
g released
1
S = 0
0 Δz (Å) 3.1
i 1
2H-site
2H-1
S = 0
S = 1/2
0 Δz (Å) 2.1
k 1
mono-H
1
S = 0
S = 0
0 Δz (Å) 2.0
f Kondo ON
h Kondo OFF
j Kondo ON
l Kondo OFF
dI/dV (arbitrary units)
-40 -20 0 20 40
Sample Bias (mV)

Figure 4